


Electron-phonon interaction and band structure renormalization using Gaussian orbital basis setsGerrit Mann¹*, Michael Rohlfing¹, and Thorsten Deilmann¹
University of Münster, Institute of Solid State Theory, 48149 Münster, Germany (Received 25 June 2024; revised 5 August 2024; accepted 9 August 2024; published 23 August 2024)

The interaction between electrons and phonons leads to a renormalization of the electronic band structure and the associated band gap. In solids this renormalization can be calculated from first principles using the supercell-based frozen phonon method or the perturbation-based Allen-Heine-Cardona theory. Each approach relies on certain assumptions and can become computationally expensive. In this work we present an *ab initio* implementation that aims to increase the accuracy and the efficiency of such calculations by combining the nonadiabatic Allen-Heine-Cardona theory and supercell calculations. Additionally, the benefits of a localized basis set of Gaussian orbitals are exploited. Due to its computational complexity the Debye-Waller component of Allen-Heine-Cardona theory is usually treated on a rigid-ion approximation level using a version of the acoustic sum rule. In our implementation the evaluation of the Debye-Waller component is straightforward and contributions beyond the rigid-ion approximation from several shells of nearest neighbors can easily be included. We use bulk silicon and diamond as test systems and find a good agreement with the literature on the level of the rigid-ion approximation. Beyond that we calculate the contributions up to third-nearest neighbors and find that these contributions are small with up to about 5% of the rigid-ion contribution but not necessarily negligible. For silicon the calculated zero-point renormalization of the direct (indirect) band gap is -43.5 meV (-54.9 meV). At high temperature, the band gaps shrink at a rate of -0.17 and -0.27 meV/K, respectively. For diamond we find a zero-point renormalization of -405.2 meV (-313.7 meV) for the direct (indirect) band gap. The reduction at high temperature is -0.46 and -0.37 meV/K, respectively.

DOI: [10.1103/PhysRevB.110.075145](https://doi.org/10.1103/PhysRevB.110.075145)**I. INTRODUCTION**

Electron-phonon interaction (EPI) provides the mechanisms that are crucial for a multitude of phenomena in solid state physics, chemistry, and material science. Some examples are conventional superconductivity, resistivity in metals, charge carrier mobility in semiconductors and insulators, the thermalization of hot carriers and the temperature dependence of optical properties [1]. However, in electronic structure calculations electron-phonon interactions are usually neglected. Most *ab initio* calculations of electronic and structural properties today employ density functional theory (DFT) [2,3], which notoriously underestimates the electronic band gap compared to experimental findings. After corrections from many-body perturbation theory (MBPT), typically in the *GW* approximation [4], the remaining mismatch between theory and experiment is in the order of 0.1 eV or below for many materials [5,6]. The renormalization of the band gap introduced by electron-phonon interaction often turns out to be of a similar size [7–9] and might therefore be able to further bridge the remaining gap between theory and experiment. Even at zero temperature the electron-phonon interaction introduces a renormalization of the electronic band structure, which is referred to as zero-point renormalization (ZPR). For rising temperature the electron-phonon renormalization (EPR)

increases in magnitude, because the occupation numbers of the phonons enter, which increase with the temperature.

Currently, two *ab initio* methods can be found in the literature that can capture such effects and are applicable to solids. Each method has its own advantages and disadvantages. The first method is the frozen phonon approach [10,11]. It is based on supercell calculations where the atoms are displaced collectively according to the patterns corresponding to specific phonon modes. The resulting changes of the band structure energies are averaged over a sufficient number of phonon modes with Bose-Einstein distributions as weights. On the one hand, it is conceptually versatile, as any electronic structure solver could be used, and several orders of electron-phonon interactions are automatically included [12]. On the other hand it is an approach that inherently relies on the adiabatic approximation [9,13] and the required supercell calculations are computationally expensive [12,13]. The second method is a perturbative approach that employs Allen-Heine-Cardona (AHC) theory [14–16] and linear response techniques in the form of density-functional perturbation theory (DFPT) [17–19]. Its treatment of electron-phonon interaction involves two contributions that are second order in electron-phonon coupling. These contributions are called the Fan-Migdal (FM) term and the Debye-Waller (DW) term. They arise from an expansion of the electron potential. This approach avoids supercells entirely and can easily incorporate nonadiabatic effects, which have shown to be important for some classes of materials [7,9]. However, it involves evaluating an integral that converges only slowly with respect to the used sampling

*Contact author: gerrit.mann@uni-muenster.de

density and is usually treated using interpolation schemes [20]. Furthermore, the evaluation of the Debye-Waller term is not straightforward but uses a variant of the acoustic sum rule [14]. Usually the rigid-ion approximation (RIA) is invoked due to the computational effort [7]. Tests of the validity of the RIA on molecules indicated that contributions beyond the RIA might not be negligible [21].

The field of *ab initio* calculations for electron-phonon interactions is comparatively young and the refinement of its methods is still continuing. Considerable efforts have been made to improve the perturbation-based [20,22–26] and supercell-based methods [12,13,23,27–31]. A major breakthrough requires implementations with high precision and low computational costs. With progress in this direction electron-phonon calculations could be adapted more widely and therefore aid in the discovery of new interesting material properties.

This work presents an attempt to advance the field in this direction. We combine the theoretical framework of nonadiabatic AHC theory with supercell calculations and exploit the benefits of a localized Gaussian basis. Previous works have already made use of localized basis sets of Wannier functions or atomic orbitals [24]. Due to their strong localization, they are well suited for Fourier interpolations, which can be used to speed up the evaluation of the occurring integral. However, we use them for a different reason as our approach does not employ interpolation schemes. Instead, replacing DFPT by supercell calculations and evaluating the required matrix elements with a basis of localized Gaussian orbitals allows us to decouple a sizable part of the computational effort from the evaluation of the slowly converging integral over the Brillouin zone. This way we obtain an implementation with a moderate computational effort such that the Debye-Waller term can be evaluated without resorting to a special treatment via the acoustic sum rule. Contributions beyond the RIA can easily be included in our calculations. Therefore, we can rigorously investigate the validity of the RIA, which was not feasible up to now, using silicon and diamond as test systems.

This paper is organized as follows. Section II reviews the common theoretical treatment of electrons and nuclei in solids. In the following Sec. III the Hamiltonians describing the first and second order of EPI are derived and the EPR from nonadiabatic AHC theory is presented. Section IV explains the practical details in the implementation of the EPR of the band structure energies. The occurring convergence behavior is presented in Sec. V. Eventually, in Sec. VI the results for the two test systems of bulk silicon and diamond are presented and our implementation is compared to previous implementations. A summary in Sec. VII will conclude the paper.

II. ELECTRONS AND PHONONS

Before turning the attention to electron-phonon interactions, it is useful to describe electrons and phonons separately. To this end, the Born-Oppenheimer approximation [32] is employed. It allows us to decouple the dynamics of electrons and nuclei. In the first step the electronic problem is solved for a fixed configuration of the nuclei, which yields the total electronic energy corresponding to this configuration. In the

second step the total electronic energy is used as a potential in the treatment of the dynamics of the nuclei.

The equilibrium position of a nucleus indicated by κ and p is given by $\tau_{\kappa p}^{(0)} = \tau_{\kappa} + \mathbf{R}_p$, where τ_{κ} is the position of the nucleus κ in the primitive unit cell and \mathbf{R}_p is the lattice vector corresponding to the unit cell with index p , and the equilibrium configuration of all atomic positions is denoted as $\{\tau_{\kappa p}^{(0)}\}$. The total electronic energy of the ground state $E_0^{\text{el}}(\{\tau_{\kappa p}^{(0)}\})$ for this equilibrium configuration can be obtained from density functional theory (DFT) calculations [2,3]. Beyond that, DFT is also commonly used as a one-body picture for the electrons. The behavior of an electron is then described by the Hamiltonian $\hat{H}^{\text{KS}} = -\frac{\hbar^2}{2m_e} \nabla^2 + V^{\text{KS}}(\mathbf{r}, \{\tau_{\kappa p}^{(0)}\})$, where the self-consistent Kohn-Sham potential V^{KS} is evaluated for the equilibrium configuration of the nuclei. In second quantization the Hamiltonian for an electron reads

$$\begin{aligned} \hat{H}_e &= \sum_{m\mathbf{k}', n\mathbf{k}} \langle \psi_{m\mathbf{k}'} | \hat{H}^{\text{KS}} | \psi_{n\mathbf{k}} \rangle \hat{c}_{m\mathbf{k}'}^\dagger \hat{c}_{n\mathbf{k}} \\ &= \sum_{n\mathbf{k}} \varepsilon_{n\mathbf{k}} \hat{c}_{n\mathbf{k}}^\dagger \hat{c}_{n\mathbf{k}}, \end{aligned} \quad (1)$$

where $\psi_{n\mathbf{k}}$ are the eigenfunctions and $\varepsilon_{n\mathbf{k}}$ are the eigenvalues of \hat{H}^{KS} [1].

For a description of the dynamics of the nuclei their positions are considered as dynamical variables. The position of each nucleus can be written in terms of a displacement from the previously fixed equilibrium position, i.e., $\tau_{\kappa p} = \tau_{\kappa p}^{(0)} + \Delta \tau_{\kappa p}$. Then the expansion of the potential up to second order around the equilibrium configuration takes the form

$$\begin{aligned} E_0^{\text{el}}(\{\tau_{\kappa p}\}) &= E_0^{\text{el}}(\{\tau_{\kappa p}^{(0)}\}) + \frac{1}{2} \sum_{\kappa\alpha p} \sum_{\kappa'\alpha'p'} \phi_{\kappa\alpha p, \kappa'\alpha'p'} \Delta \tau_{\kappa\alpha p} \Delta \tau_{\kappa'\alpha'p'} \\ &\quad + \mathcal{O}(\{\Delta \tau_{\kappa\alpha p}\}^3), \end{aligned} \quad (2)$$

with force constants $\phi_{\kappa\alpha p, \kappa'\alpha'p'}$ defined as the second-order derivatives of E_0^{el} with respect to $\tau_{\kappa\alpha p}$ and $\tau_{\kappa'\alpha'p'}$ evaluated for the nuclear positions in equilibrium [33]. The index $\alpha = x, y, z$ denotes the Cartesian components. Within the harmonic approximation only terms up to second order in the atomic displacements are considered leading to a system of coupled harmonic oscillators. Decoupling them requires to solve the eigenvalue problem

$$\sum_{\kappa'\alpha'} D_{\kappa\alpha, \kappa'\alpha'}(\mathbf{q}) e_{\kappa'\alpha', v}(\mathbf{q}) = \omega_{\mathbf{q}, v}^2 e_{\kappa\alpha, v}(\mathbf{q}) \quad (3)$$

with the dynamical matrix $D_{\kappa\alpha, \kappa'\alpha'}(\mathbf{q})$ given by

$$D_{\kappa\alpha, \kappa'\alpha'}(\mathbf{q}) = \sum_p e^{i\mathbf{q}\cdot\mathbf{R}_p} \frac{\phi_{\kappa\alpha 0, \kappa'\alpha' p}}{\sqrt{M_\kappa M_{\kappa'}}}, \quad (4)$$

where M_κ is the mass of the corresponding nucleus κ [33]. Solving the eigenvalue problem yields decoupled normal modes $e_{\kappa\alpha, v}(\mathbf{q})$ with vibrational frequencies $\omega_{\mathbf{q}, v}$. Each mode is characterized by a wave vector \mathbf{q} and a branch index v . Expressed in the language of second quantization, the Hamiltonian of the phonons within the harmonic approximation

reads [1]

$$\hat{H}_p = \sum_{\mathbf{q}\nu} \hbar\omega_{\mathbf{q}\nu} \left(\hat{a}_{\mathbf{q}\nu}^\dagger \hat{a}_{\mathbf{q}\nu} + \frac{1}{2} \right). \quad (5)$$

III. ELECTRON-PHONON INTERACTION IN DENSITY FUNCTIONAL THEORY

Equation (1) describes the electrons for a rigid atomic configuration. However, all effects on the electronic properties that result from electron-phonon interaction are lost when fixed atomic positions are assumed. The strategy presented in this section is to recover the effects of electron-phonon interaction in DFT calculations by treating the term that is neglected by this assumption as a perturbation. Starting from this approach the Hamiltonians describing the first and second order of electron-phonon interactions are derived. These can then be treated within perturbation theory in order to obtain the renormalization of the electronic band structure energies. The final renormalization is obtained after making minor modifications arising from many-body theory.

In DFT the aforementioned perturbation reads $V^{\text{KS}}(\mathbf{r}, \{\boldsymbol{\tau}_{\kappa p}\}) - V^{\text{KS}}(\mathbf{r}, \{\boldsymbol{\tau}_{\kappa p}^{(0)}\})$. Since its explicit form is not known, it is expanded up to second order around the fixed configuration of the nuclei to capture its main contributions. The expansion takes the form

$$\begin{aligned} V^{\text{KS}}(\mathbf{r}, \{\boldsymbol{\tau}_{\kappa p}\}) - V^{\text{KS}}(\mathbf{r}, \{\boldsymbol{\tau}_{\kappa p}^{(0)}\}) &= \sum_{\kappa\alpha p} \frac{\partial V^{\text{KS}}}{\partial \tau_{\kappa\alpha p}} \Delta\tau_{\kappa\alpha p} \\ &+ \frac{1}{2} \sum_{\kappa\alpha p} \sum_{\kappa'\alpha' p'} \frac{\partial^2 V^{\text{KS}}}{\partial \tau_{\kappa\alpha p} \partial \tau_{\kappa'\alpha' p'}} \Delta\tau_{\kappa\alpha p} \Delta\tau_{\kappa'\alpha' p'} \\ &+ \mathcal{O}(\{\Delta\tau_{\kappa\alpha p}\}^3), \end{aligned} \quad (6)$$

where the derivatives are evaluated at the equilibrium configuration of the nuclei [1]. Using the normal modes, the atomic displacements in this expansion can be rewritten as

$$\Delta\tau_{\kappa\alpha p} = \sum_{\mathbf{q}\nu} \sqrt{\frac{\hbar}{2M_\kappa\omega_{\mathbf{q}\nu}N_{\text{uc}}}} e_{\kappa\alpha,\nu}(\mathbf{q}) e^{i\mathbf{q}\cdot\mathbf{R}_p} (\hat{a}_{-\mathbf{q}\nu}^\dagger + \hat{a}_{\mathbf{q}\nu}), \quad (7)$$

where N_{uc} is the number of unit cells in the considered Born-von-Kármán cell [1]. The first- and second-order terms of the expansion are added to the Hamiltonian \hat{H}^{KS} in Eq. (1). In order to write the additional parts more conveniently, the matrix elements

$$g_{m\nu\nu'}^{\text{FM}}(\mathbf{k}, \mathbf{q}) = \langle u_{m\mathbf{k}+\mathbf{q}} | \Delta_{\mathbf{q}\nu} v^{\text{KS}} | u_{n\mathbf{k}} \rangle_{\text{uc}}, \quad (8)$$

$$g_{m\nu\nu'}^{\text{DW}}(\mathbf{k}, \mathbf{q}, \mathbf{q}') = \frac{1}{2} \langle u_{m\mathbf{k}+\mathbf{q}+\mathbf{q}'} | \Delta_{\mathbf{q}\nu} \Delta_{\mathbf{q}'\nu'} v^{\text{KS}} | u_{n\mathbf{k}} \rangle_{\text{uc}}, \quad (9)$$

are defined, where $u_{n\mathbf{k}}$ is the lattice periodic part in $\psi_{n\mathbf{k}}(\mathbf{r}) = N_{\text{uc}}^{-1/2} u_{n\mathbf{k}}(\mathbf{r}) e^{i\mathbf{k}\cdot\mathbf{r}}$. The operators in the brackets are given by [1]

$$\Delta_{\mathbf{q}\nu} v^{\text{KS}} = \sum_{\kappa\alpha} \sqrt{\frac{\hbar}{2M_\kappa\omega_{\mathbf{q}\nu}}} e_{\kappa\alpha,\nu}(\mathbf{q}) \partial_{\kappa\alpha,\mathbf{q}} v^{\text{KS}}, \quad (10)$$

$$\begin{aligned} \Delta_{\mathbf{q}\nu} \Delta_{\mathbf{q}'\nu'} v^{\text{KS}} &= \frac{\hbar}{2} \sum_{\kappa\alpha} \sum_{\kappa'\alpha'} \frac{e_{\kappa\alpha,\nu}(\mathbf{q}) e_{\kappa'\alpha',\nu'}(\mathbf{q}')}{\sqrt{M_\kappa M_{\kappa'} \omega_{\mathbf{q}\nu} \omega_{\mathbf{q}'\nu'}}} \\ &\times \partial_{\kappa\alpha,\mathbf{q}} \partial_{\kappa'\alpha',\mathbf{q}'} v^{\text{KS}} \end{aligned} \quad (11)$$

with

$$\partial_{\kappa\alpha,\mathbf{q}} v^{\text{KS}} = \sum_p e^{-i\mathbf{q}\cdot(\mathbf{r}-\mathbf{R}_p)} \frac{\partial V^{\text{KS}}}{\partial \tau_{\kappa\alpha p}} \quad \text{and} \quad (12)$$

$$\begin{aligned} \partial_{\kappa\alpha,\mathbf{q}} \partial_{\kappa'\alpha',\mathbf{q}'} v^{\text{KS}} &= \sum_{p,p'} e^{-i\mathbf{q}\cdot(\mathbf{r}-\mathbf{R}_p)} e^{-i\mathbf{q}'\cdot(\mathbf{r}-\mathbf{R}_{p'})} \\ &\times \frac{\partial^2 V^{\text{KS}}}{\partial \tau_{\kappa\alpha p} \partial \tau_{\kappa'\alpha' p'}}. \end{aligned} \quad (13)$$

After defining these quantities, the parts of the Hamiltonian that describe electron-phonon interactions read [1]

$$\hat{H}_{\text{ep}}^{(1)} = N_{\text{uc}}^{-1/2} \sum_{\mathbf{k},\mathbf{q}} \sum_{m\nu\nu'} g_{m\nu\nu'}^{\text{FM}}(\mathbf{k}, \mathbf{q}) \hat{c}_{m\mathbf{k}+\mathbf{q}}^\dagger \hat{c}_{n\mathbf{k}} (\hat{a}_{-\mathbf{q}\nu}^\dagger + \hat{a}_{\mathbf{q}\nu}), \quad (14)$$

$$\begin{aligned} \hat{H}_{\text{ep}}^{(2)} &= N_{\text{uc}}^{-1} \sum_{\mathbf{k},\mathbf{q},\mathbf{q}'} \sum_{m\nu\nu'} g_{m\nu\nu'}^{\text{DW}}(\mathbf{k}, \mathbf{q}, \mathbf{q}') \hat{c}_{m\mathbf{k}+\mathbf{q}+\mathbf{q}'}^\dagger \hat{c}_{n\mathbf{k}} \\ &\times (\hat{a}_{-\mathbf{q}\nu}^\dagger + \hat{a}_{\mathbf{q}\nu}) (\hat{a}_{-\mathbf{q}'\nu'}^\dagger + \hat{a}_{\mathbf{q}'\nu'}). \end{aligned} \quad (15)$$

The Hamiltonian $\hat{H}_{\text{ep}}^{(1)}$ describes interactions between an electron and one phonon, whereas $\hat{H}_{\text{ep}}^{(2)}$ describes interactions between an electron and two phonons.

The perturbations $\hat{H}_{\text{ep}}^{(1)}$ and $\hat{H}_{\text{ep}}^{(2)}$ to the DFT Hamiltonian of an electron are assumed to be small. Applying perturbation theory for static displacements of the nuclei yields the formula for the renormalization of the electronic band structure found by Allen and Heine [14]. However, such a treatment relies on the adiabatic approximation and does not capture the dynamical nature of the atomic displacements [34]. Alternatively, the problem can be treated within a more advanced many-body formalism as summarized in Ref. [1]. For practical calculations this formalism can be merged with DFT calculations [35]. After several approximations the field-theoretic approach yields the Fan-Migdal component,

$$\begin{aligned} \Delta E_{n\mathbf{k}}^{\text{FM}} &= \sum_\nu \int \sum_m |g_{m\nu\nu'}^{\text{FM}}(\mathbf{k}, \mathbf{q})|^2 \left[\frac{1 - f_{m\mathbf{k}+\mathbf{q}} + n_{\mathbf{q}\nu}}{\varepsilon_{n\mathbf{k}} - \varepsilon_{m\mathbf{k}+\mathbf{q}} - \hbar\omega_{\mathbf{q}\nu}} \right. \\ &\left. + \frac{f_{m\mathbf{k}+\mathbf{q}} + n_{\mathbf{q}\nu}}{\varepsilon_{n\mathbf{k}} - \varepsilon_{m\mathbf{k}+\mathbf{q}} + \hbar\omega_{\mathbf{q}\nu}} \right] \frac{d\mathbf{q}}{\Omega_{\text{BZ}}}, \end{aligned} \quad (16)$$

and the Debye-Waller component,

$$\Delta E_{n\mathbf{k}}^{\text{DW}} = \sum_\nu \int g_{m\nu\nu'}^{\text{DW}}(\mathbf{k}, \mathbf{q}, -\mathbf{q}) (2n_{\mathbf{q}\nu} + 1) \frac{d\mathbf{q}}{\Omega_{\text{BZ}}}, \quad (17)$$

to the renormalization of the electronic band structure, where $f_{m\mathbf{k}+\mathbf{q}}$ is the Fermi-Dirac distribution for an electron with the energy $\varepsilon_{m\mathbf{k}+\mathbf{q}}$ and $n_{\mathbf{q}\nu}$ is the Bose-Einstein distribution for a phonon with the energy $\hbar\omega_{\mathbf{q}\nu}$ [1]. The renormalized band structure energy is then given by

$$E_{n\mathbf{k}} = \varepsilon_{n\mathbf{k}} + \Delta E_{n\mathbf{k}}^{\text{FM}} + \Delta E_{n\mathbf{k}}^{\text{DW}}. \quad (18)$$

This result agrees with the adiabatic Allen-Heine formula when the phonon energies in the denominators are neglected [34].

IV. IMPLEMENTATION

In general applying the previously described theory directly to the systems of interest is not feasible. For a practical implementation further techniques are required. This section outlines the details of the calculations based on the theory from Secs. II and III.

The DFT calculations for the electronic structure employ an exchange-correlation functional. In this work we use the parametrization of Perdew and Zunger [36] of the local density approximation (LDA). This functional is chosen as it has proven to be well suited for describing vibrational properties [37]. Furthermore, we use norm-conserving *ab initio* pseudopotentials [38–42]. Our implementation employs a basis set of localized orbitals, i.e., we use Bloch basis functions of the form

$$f_{\beta\kappa}^{\mathbf{k}}(\mathbf{r}) = \sum_p e^{i\mathbf{k}\cdot\boldsymbol{\tau}_{\kappa p}} \varphi_{\beta\kappa}(\mathbf{r} - \boldsymbol{\tau}_{\kappa p}), \quad (19)$$

where $\varphi_{\beta\kappa}(\mathbf{r} - \boldsymbol{\tau}_{\kappa p})$ are localized Gaussian orbitals centered at $\boldsymbol{\tau}_{\kappa p}$, in order to represent the DFT wave function as

$$\psi_{n\mathbf{k}}(\mathbf{r}) = \frac{1}{\sqrt{N_{\text{uc}}}} \sum_{\beta\kappa} c_{\beta\kappa}^{n\mathbf{k}} f_{\beta\kappa}^{\mathbf{k}}(\mathbf{r}) \quad (20)$$

with coefficients $c_{\beta\kappa}^{n\mathbf{k}}$. For the calculation of the force constants that are required to determine the phonon dispersion a finite-differences approach similar to the approaches described in Refs. [43,44] is used.

The central quantities for the calculation of the EPR are the matrix elements $g_{mnv}^{\text{FM}}(\mathbf{k}, \mathbf{q})$ and $g_{mnv}^{\text{DW}}(\mathbf{k}, \mathbf{q}, -\mathbf{q})$ of the electron-phonon coupling. They contain the first- and second-order derivatives of the Kohn-Sham potential. In our implementation, these are calculated in a finite-differences approach that will be described in the following. Engel *et al.* [44] utilized finite differences calculations in a similar way to calculate the EPR of electronic band structures. Gunst *et al.* [45] used an approach that is similar to our approach to evaluate the matrix element $g_{mnv}^{\text{FM}}(\mathbf{k}, \mathbf{q})$, which were then used for other physical quantities. We emphasize here that the techniques employed in our approach can also be reused for a multitude of properties related to electron-phonon interactions that involve the evaluation of the aforementioned matrix elements. Exploiting the lattice periodicity of the Kohn-Sham potential V^{KS} , we can write

$$\langle u_{m\mathbf{k}+\mathbf{q}} | \partial_{\kappa\alpha} \mathbf{q} v^{\text{KS}} | u_{n\mathbf{k}} \rangle_{\text{uc}} = \langle u_{m\mathbf{k}+\mathbf{q}} | e^{-i\mathbf{q}\cdot\mathbf{r}} \frac{\partial V^{\text{KS}}}{\partial \tau_{\kappa\alpha 0}} | u_{n\mathbf{k}} \rangle, \quad (21)$$

$$\begin{aligned} \langle u_{n\mathbf{k}} | \partial_{\kappa\alpha} \mathbf{q} \partial_{\kappa'\alpha'} -\mathbf{q} v^{\text{KS}} | u_{n\mathbf{k}} \rangle_{\text{uc}} \\ = \sum_p e^{-i\mathbf{q}\cdot\mathbf{R}^p} \langle u_{n\mathbf{k}} | \frac{\partial^2 V^{\text{KS}}}{\partial \tau_{\kappa\alpha 0} \partial \tau_{\kappa'\alpha' p}} | u_{n\mathbf{k}} \rangle, \end{aligned} \quad (22)$$

where the unit cell index 0 refers to the reference unit cell. Combining the lattice periodicity of the Kohn-Sham potential with the symmetry of second-order derivatives yields the relation

$$\langle u_{n\mathbf{k}} | \frac{\partial^2 V^{\text{KS}}}{\partial \tau_{\kappa\alpha 0} \partial \tau_{\kappa'\alpha' p}} | u_{n\mathbf{k}} \rangle = \langle u_{n\mathbf{k}} | \frac{\partial^2 V^{\text{KS}}}{\partial \tau_{\kappa'\alpha' 0} \partial \tau_{\kappa\alpha (0-p)}} | u_{n\mathbf{k}} \rangle, \quad (23)$$

reducing the number of required derivatives even further, where the index $(0-p)$ corresponds to the lattice vector $-\mathbf{R}_p$. The specific crystal symmetry of the considered system does not enter. The derivatives of V^{KS} are evaluated using a finite-differences approach. That means a supercell is set up where the relevant atoms are displaced by a small amount ε in the order of 5 mÅ and the Kohn-Sham equations are again solved self-consistently. A sufficiently large basis set ensures that the slight shift of the basis functions is negligible [46,47]. Taking the finite-differences quotient of the Kohn-Sham potentials resulting from different atomic configurations yields an approximation for the corresponding derivatives. The same strategy of using finite differences is applied to the nonlocal part of the pseudopotential. For the finite differences, we employ the central differences formulas both in the case of first- and second-order derivatives. The displacements for the first-order derivatives are reused for mixed second-order derivatives. In each case the truncation error is of the order $\mathcal{O}(\varepsilon^2)$. Note that this procedure requires calculations with $6N$ configurations for the first-order derivatives and additional $1 + 6N$ configurations for the second-order derivatives considered in the RIA. Here N denotes the number of atoms in the unit cell. For the contributions from nearest neighbors further configurations have to be considered, their number still scales linearly with N for a fixed number of nearest neighbors. These additional configurations also include displacements of single atoms that are not contained in the reference unit cell. Finally, we are interested in the limit of infinitely large supercells. Since the numerical evaluation for an infinitely large supercell is unfeasible, the size of the supercell becomes a convergence parameter.

The matrix elements are evaluated using the wave functions of the unperturbed atomic configuration. This requires evaluating

$$\begin{aligned} \int f_{\beta_1\kappa_1}^{\mathbf{k}+\mathbf{q}*}(\mathbf{r}) \frac{\partial V^{\text{KS}}}{\partial \tau_{\kappa\alpha 0}} f_{\beta_2\kappa_2}^{\mathbf{k}}(\mathbf{r}) d\mathbf{r} \\ = \sum_{p_1, p_2} e^{i\mathbf{k}\cdot\boldsymbol{\tau}_{\kappa_2 p_2}} e^{-i(\mathbf{k}+\mathbf{q})\cdot\boldsymbol{\tau}_{\kappa_1 p_1}} \int \varphi_{\beta_1\kappa_1}^*(\mathbf{r} - \boldsymbol{\tau}_{\kappa_1 p_1}) \\ \times \frac{\partial V^{\text{KS}}}{\partial \tau_{\kappa\alpha 0}} \varphi_{\beta_2\kappa_2}(\mathbf{r} - \boldsymbol{\tau}_{\kappa_2 p_2}) d\mathbf{r} \end{aligned} \quad (24)$$

and

$$\begin{aligned} \int f_{\beta_1\kappa_1}^{\mathbf{k}*}(\mathbf{r}) \frac{\partial^2 V^{\text{KS}}}{\partial \tau_{\kappa\alpha 0} \partial \tau_{\kappa'\alpha' p}} f_{\beta_2\kappa_2}^{\mathbf{k}}(\mathbf{r}) d\mathbf{r} \\ = \sum_{p_1, p_2} e^{i\mathbf{k}\cdot(\boldsymbol{\tau}_{\kappa_2 p_2} - \boldsymbol{\tau}_{\kappa_1 p_1})} \int \varphi_{\beta_1\kappa_1}^*(\mathbf{r} - \boldsymbol{\tau}_{\kappa_1 p_1}) \\ \times \frac{\partial^2 V^{\text{KS}}}{\partial \tau_{\kappa\alpha 0} \partial \tau_{\kappa'\alpha' p}} \varphi_{\beta_2\kappa_2}(\mathbf{r} - \boldsymbol{\tau}_{\kappa_2 p_2}) d\mathbf{r}. \end{aligned} \quad (25)$$

Here the advantage of the basis set of localized orbitals becomes evident. The matrix elements of the Bloch basis have to be evaluated for a large number of wave vectors \mathbf{q} and \mathbf{k} . However, the matrix elements of the Gaussian basis do not depend on them and thus, they only have to be calculated once and can be stored in memory for later reuse.

When the latter matrix elements are calculated, it is important to note that the derivatives exhibit supercell periodicity and that the integral has to be taken only over this supercell and not the entire space. In our implementation the corresponding integral is evaluated analytically using the Fourier representation of the derivatives of the potential [48]. This procedure assumes that the integral is taken over the entire space. In order not to capture the supercell-periodic repetitions of the derivatives, only Gaussians with specifically positioned centers are included. For the first-order derivatives Gaussians with centers inside a sphere around the displaced atom are considered, where the radius of this sphere is half of the distance to the nearest supercell-periodic repetition of the displaced atom. The case of the second-order derivatives, taken with respect to the positions of *two* atoms, is treated similarly. Here a sphere of the same radius is used, which is centered at the midpoint between the two atoms.

A crucial point in the evaluation of the Fan-Migdal component is the integral $\int d\mathbf{q}$ due to the contributions where the denominator $\varepsilon_{n\mathbf{k}} - \varepsilon_{m\mathbf{k}+\mathbf{q}} \pm \hbar\omega_{\mathbf{q}\nu}$ is close to zero. These lead to a slow convergence of the integral with respect to the density of the \mathbf{q} -point sampling [49]. In order to mitigate this problem, an imaginary part $i\delta$ is commonly introduced to the denominator, where δ is often chosen as a value of about 100 meV [49–52] and may be extrapolated to zero [7]. The physical result is finally obtained by taking the real part. This imaginary part can be justified theoretically as a finite lifetime of the electronic states [50]. A corresponding term also appears within a MBPT approach in the form of the imaginary part of the electron self-energy [1].

V. NUMERICAL DETAILS

Before we discuss the results in Sec. VI, we need to ensure their convergence in our approach. The critical numerical parameters include in particular the basis set, the supercell size, the sampling of the \mathbf{q} -point grid, the convergence parameter δ , the finite-differences displacement ε , and the convergence of the Kohn-Sham potential. Since the numerical convergence of silicon and diamond is similar, we restrict ourselves to diamond. A comparison to previous implementations and the discussion of the computational effort conclude this section.

A. Basis set and supercell size

Equation (16) contains a sum over bands m , which runs to infinity. The number of bands used for the evaluation of this sum in numerical calculations is a convergence parameter. In plane-wave calculations a large number of bands might be required to achieve convergence [51]. This problem can be solved by using methods based on solving a Sternheimer equation for the unoccupied bands [21] or by resorting to Wannier function perturbation theory [26]. In our implementation using a basis of localized orbitals none of these techniques is employed and we sum over all bands of the corresponding basis set. Thus, the size of the basis set is connected to this convergence parameter as well as to the accuracy in the evaluation of the matrix elements in Eqs. (24) and (25). Figure 1 shows the dependence of the FM component of the ZPR on the size of our Gaussian-orbital

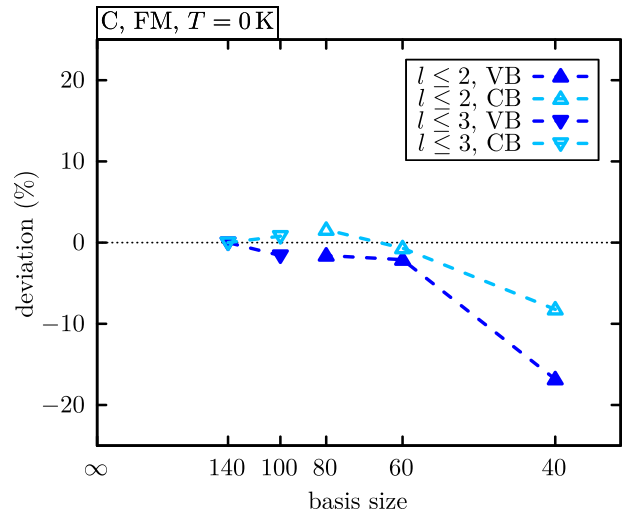


FIG. 1. The convergence behavior of the FM component of the ZPR at the Γ point for the highest valence band (VB) and the lowest conduction band (CB) in diamond using orbitals with angular momentum character $l \leq 2$ and $l \leq 3$. The relative deviation is calculated with respect to the results for the largest basis set and the lines are a guide to the eye.

basis. The highest state of the valence band and the lowest state of the conduction band at the Γ point in diamond are shown as examples. The basis sets with $l \leq 2$ comprise orbital types s , p , d , and s^* . Basis sets with $l \leq 3$ also include f and p^* orbitals. We note in passing that these have been left out for the orbitals with the smallest decay constant, i.e., the most delocalized orbitals, to maintain the numerical stability of the overlap matrix. The relative deviation is calculated with respect to the results for the largest basis set. We find a sufficient convergence with 60 basis functions in diamond. The investigations for silicon, which are not shown here, yield a sufficient convergence for 100 basis functions. Similar convergence studies have also been carried out for the DW component, which converges even faster.

In our approach the evaluation of the derivative of the Kohn-Sham potential is based on supercell calculations where the size of the supercell is a convergence parameter. The convergence with respect to the supercell size for the FM and DW components of the ZPR of the electronic band structure in diamond is presented in Fig. 2. Supercells of the form $N_{sc} \times N_{sc} \times N_{sc}$ are assumed. In these calculations the DW component includes terms up to first-nearest neighbors. The states at the Γ point for the highest valence band and the lowest conduction band are chosen as representative examples. All data points are represented in terms of their relative deviation from the corresponding results in a $7 \times 7 \times 7$ supercell. Among the calculated data points the FM component converges monotonically, whereas the DW component shows an oscillating behavior. Considering the small size of the relative deviations a $5 \times 5 \times 5$ supercell seems to be sufficient.

We note that in polar or infrared-active materials long-range electron-phonon couplings may become important. Ponc e *et al.* [7] pointed out that the long-range electron-phonon interactions in polar materials lead to an unphysical divergence of the adiabatic renormalization. They solved this

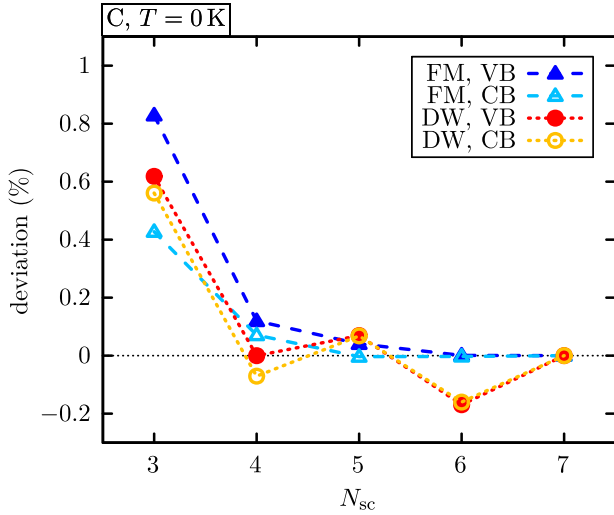


FIG. 2. The convergence behavior of the FM and the DW component of the ZPR at the Γ point for the highest valence band (VB) and the lowest conduction band (CB) in diamond including contributions to the DW term up to first-nearest neighbors. The relative deviation is calculated with respect to the results for a $7 \times 7 \times 7$ supercell and the lines are a guide to the eye.

problem by switching to the nonadiabatic renormalization, where the phonon energies are included in the energy differences of the denominators of the FM component as it is done in our approach. Still, the long-range interactions might lead to large supercell sizes in our approach. Similarly to previous methods [7,12] this could increase the numerical effort significantly. Fröhlich contributions are usually added explicitly [53,54] and could be added analogously to our implementation. However, since the materials discussed in this work are nonpolar, we postpone this discussion to future work.

B. Sampling of the \mathbf{q} -point grid

The convergence of the integral $\int d\mathbf{q}$ with respect to the sampling of the \mathbf{q} points is a critical detail that is inherent to any approach that employs the presented underlying theory. We start with the discussion of the DW term and come to the more tricky FM term afterwards. Figure 3 displays the convergence of the DW component at the Γ point for the highest valence band and the lowest conduction band of diamond with respect to the density of the \mathbf{q} -point grid of the form $N_q \times N_q \times N_q$. The DW component includes contributions up to first-nearest neighbors and the relative deviation is calculated with respect to the corresponding results for a grid of $50 \times 50 \times 50$ \mathbf{q} points. From Fig. 3 it becomes apparent that a grid of $30 \times 30 \times 30$ \mathbf{q} points is sufficiently dense for the DW component.

Similar convergence studies for the FM component have to be carried out in dependence of the convergence parameter δ as the expression for ΔE_{nk}^{FM} [Eq. (18)] contains contributions with energy denominators that approach zero. Figure 4 shows the convergence behavior of the FM component, again at the Γ point for the highest valence band and the lowest conduction band of diamond, with respect to the density of the \mathbf{q} -point grid of the form $N_q \times N_q \times N_q$ in dependence of the conver-

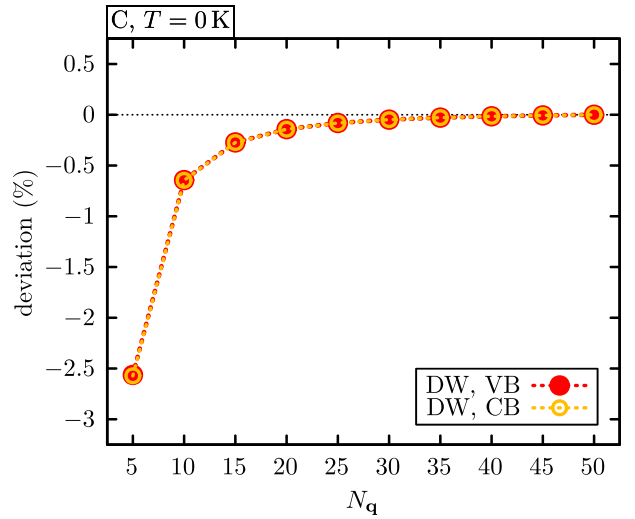


FIG. 3. The convergence behavior of the DW component of the ZPR at the Γ point for the highest valence band (VB) and the lowest conduction band (CB) in diamond including contributions to the DW term up to first-nearest neighbors. The relative deviation is calculated with respect to the results for a $50 \times 50 \times 50$ grid of \mathbf{q} points and the lines are a guide to the eye.

gence parameter δ . The relative deviations are calculated with respect to the corresponding results for a $50 \times 50 \times 50$ grid of \mathbf{q} points with $\delta = 1 \times 10^{-2}$ Ryd. For the highest valence band in Fig. 4(a) the convergence behavior is smooth for all shown choices of δ . It can also be seen that increasing δ shifts the limit with respect to the \mathbf{q} -point sampling. The case of the lowest conduction band in Fig. 4(b) is similar in regards to the latter. However, if δ is chosen too small there, then the convergence with respect to the density of \mathbf{q} points becomes inconveniently slow and less controlled. As the goal is to choose δ such that convergence is achieved for a reasonable number of \mathbf{q} points while the limit with respect to the \mathbf{q} -point sampling does not shift too much, we choose $\delta = 1 \times 10^{-2}$ Ryd. It fulfills both requirements and the corresponding results are sufficiently converged for a grid of $30 \times 30 \times 30$ \mathbf{q} points.

C. Accuracy of finite differences

Another critical point in our finite-differences approach is the convergence of the Kohn-Sham potential. Decreasing the finite displacement ε diminishes the truncation error that occurs when the derivative is replaced by a finite difference. However, the finite-differences formula for the second-order derivatives is applied to the numerical approximations of the Kohn-Sham potential for different atomic configurations and therefore there is a numerical error in the numerator that is divided by ε^2 in the denominator. Thus, the numerical error in the Kohn-Sham potentials is scaled up significantly for small finite displacements ε . Thus, decreasing the finite displacement ε in order to improve the accuracy of the derivative should go hand in hand with improving the convergence of the Kohn-Sham potential accordingly, which is controlled by the convergence threshold ΔV_{\max}^2 that provides the termination criterion $|V_{in} - V_{out}|^2 < \Delta V_{\max}^2$ for the electronic

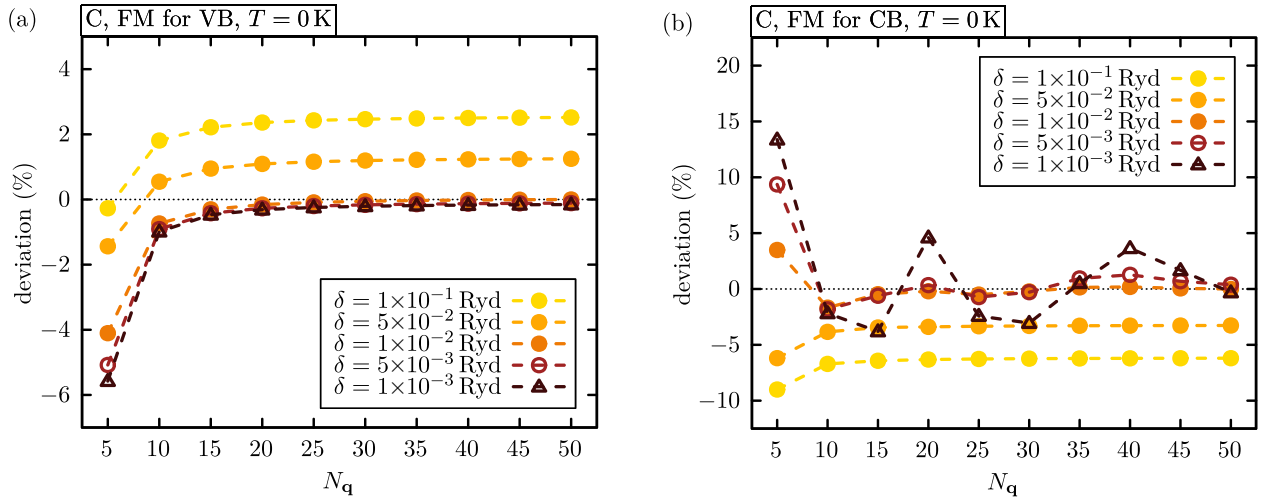


FIG. 4. The convergence behavior of the FM component of the ZPR at the Γ point for (a) the highest valence band (VB) and (b) the lowest conduction band (CB) in diamond. The relative deviations are calculated with respect to the results for a $50 \times 50 \times 50$ grid of \mathbf{q} points with $\delta = 1 \times 10^{-2}$ Ryd and the values of δ in the key are given in atomic Rydberg units. The lines are a guide to the eye.

self-consistency iterations. The issue is analyzed in Fig. 5, which shows the convergence of the DW component, again at the Γ point for the highest valence band and the lowest conduction band in diamond, respectively, with respect to the convergence threshold ΔV_{\max}^2 of the Kohn-Sham potential and for different finite displacements ε . The DW component includes contributions up to first-nearest neighbors and the relative deviation is calculated with respect to the corresponding results with a convergence threshold of $\Delta V_{\max}^2 = 10^{-22}$ Ryd² combined with a finite displacement of $\varepsilon = 1 \times 10^{-2} a_B$. The figures make the reduction of the truncation error visible as ε is decreased. A finite displacement of $\varepsilon = 1 \times 10^{-2} a_B$ converges the DW component sufficiently. A convergence threshold of $\Delta V_{\max}^2 = 10^{-16}$ Ryd² seems to be suitable. For the FM component the same discussion can be held. However, the fact that only first-order derivatives are required

there and that the denominator of the corresponding finite-differences formula scales like ε instead of ε^2 mitigates the issue.

D. Computational requirements

For silicon and diamond we find a good agreement with the numerical results from previous implementations as discussed in the following section. At the same time we retain a moderate computational effort by combining supercell calculations and a basis set of localized Gaussian orbitals with the nonadiabatic AHC theory. The size of the supercells is a convergence parameter in our approach, which appears to be rather limited as a $5 \times 5 \times 5$ supercell is sufficient for the considered test systems. At the same time the number of supercell calculations is fixed by the desired number of derivatives to include in the calculation. Both the number and the size of the supercells to consider do not depend on the sampling of phonon

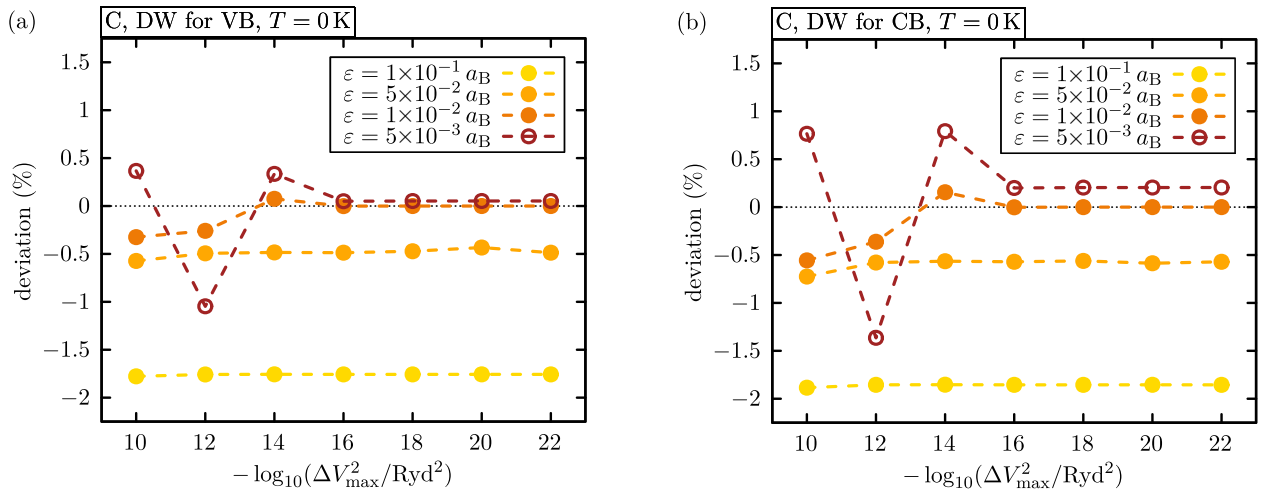


FIG. 5. The convergence of the DW component of the ZPR at the Γ point for (a) the highest valence band (VB) and (b) the lowest conduction band (CB) in diamond including contributions to the DW term up to first-nearest neighbors. The relative deviations are calculated with respect to the results for a convergence threshold of $\Delta V_{\max}^2 = 10^{-22}$ Ryd² with a displacement of $\varepsilon = 1 \times 10^{-2} a_B$. The values of ε in the key are given in atomic Rydberg units and the lines are a guide to the eye.

modes. Therefore, we circumvent the original computational bottleneck of the frozen-phonon method. Note that in the current state-of-the-art implementations of the frozen-phonon method the number of required supercell calculations has been reduced drastically. By employing the special displacement approach [13], it is sufficient to carry out one calculation in a huge supercell. Beyond that, using supercell calculations instead of DFPT makes the evaluation of the DW term in AHC theory conceptually simple as applying the acoustic sum rule is not required. The crucial point of our implementation is combining the supercell calculations with a basis set of localized Gaussian orbitals. The derivatives of the Kohn-Sham potential and their matrix elements in the Gaussian basis are independent of the wave vector \mathbf{q} . Therefore, they are completely decoupled from the \mathbf{q} -point integration contained in AHC theory and only have to be evaluated once. The \mathbf{q} -point integration can then be carried out efficiently as a weighted sum of these matrix elements where the weights depend on \mathbf{q} only via phase factors, the properties of the phonon modes corresponding to this wave vector and the properties of the electrons scattered by it. With this we circumvent the original bottleneck of DFPT calculations of AHC theory. Note that this bottleneck is less critical in current state-of-the-art DFPT + AHC theory implementations due to the use of Fourier interpolations [55,56] or Wannier function perturbation theory [26]. Therefore, our implementation is among the most efficient implementations of EPR calculations. Additionally, in our implementation contributions from several shells of nearest neighbors beyond the RIA, which are usually neglected due to the associated computational effort, can easily be included.

We note in passing, that the off-diagonal DW terms as they have been discussed within the RIA by Lihm *et al.* [25] can easily be calculated in our approach as our method does not invoke translational invariance at any point. However, since the off-diagonal DW terms are mostly relevant for temperature-driven topological transitions [25], which are not considered here, they are not evaluated for the materials considered in this work.

Computations in our approach can be split into two parts. In the first part the supercell calculations are performed and the required derivatives of the Kohn-Sham potential are stored to the disk. In the second part the EPR is evaluated. The computation time depends on the number of computed derivatives and therefore on the number of considered shells of nearest neighbors. For silicon and diamond the number of performed supercell calculations is 25, 115, 385, and 637 for contributions up to the RIA and first-, second-, and third-nearest neighbors, respectively. In the case of silicon the associated computational effort for fully converged results is 660, 3.030, 10.150, and 16.800 core hours, respectively. The subsequent evaluation of the fully converged EPR up to third-nearest neighbors requires additional 6.400 core hours on a Skylake (Gold 6140) CPU architecture with 2.30 GHz if no symmetries are exploited in the evaluation of the \mathbf{q} -point integral. However, even with a total computation time of less than 100 core hours it is possible to obtain physically reasonable results. Thus, we suggest that our method might be very suitable for performing electron-phonon calculations in large and intricate systems.

VI. RESULTS AND DISCUSSION

In this section we present the results obtained from applying our methods to the test systems of bulk silicon and diamond. These are then compared to results from other implementations in the literature in order to validate the accuracy of our calculations. As previous calculations based on the AHC theory relied on the RIA, we can use our results to investigate the importance of contributions up to third-nearest neighbors beyond the RIA for the electron-phonon renormalization of the electronic band structure and its associated band gap. After the discussion in the previous Sec. V, we conclude that a $5 \times 5 \times 5$ supercell, $\delta = 1 \times 10^{-2}$ Ryd with a grid of $30 \times 30 \times 30$ \mathbf{q} points, and a finite displacement of $\varepsilon = 1 \times 10^{-2} a_B$ with a convergence threshold of $\Delta V_{\max}^2 = 10^{-16}$ Ryd² for the Kohn-Sham potential is sufficient in order to yield converged results. These parameters are used in all electron-phonon calculations presented in this section.

A. Silicon

The results of the electron-phonon calculations for silicon have been obtained using a basis set of Gaussians with three different decay constants. For the smallest decay constant, i.e., the most delocalized Gaussians, we use orbital types s , p , d , and s^* ($l \leq 2$). For the other decay constants we also add the orbital types f and p^* ($l = 3$). Thus our basis set corresponds at least to a triple ζ -polarized basis set. This choice retains the numerical stability of the overlap matrix while making the basis set more flexible for a description of unoccupied states. The basis set then consists of the discussed Gaussian orbitals centered at each atom in the unit cell. We find a relaxed lattice parameter of 5.391 Å. This is 0.7% smaller than the experimental findings of 5.431 Å [57].

The electronic band structure of bulk silicon is depicted in Fig. 6(a). It exhibits a direct band gap of 2.557 eV and an indirect band gap of 0.448 eV. These underestimate the band gap compared to many-body calculations [58] and experiments [59], which is common for DFT calculations. The phonon dispersion of silicon is shown in Fig. 6(b). We find an agreement of up to about 5 meV with previous calculations [60,61] and measurements [62–64].

In Fig. 7 the colors on top of the original DFT band structure of silicon indicate the sign and the size of the EPR calculated using Eq. (18). For this calculation temperatures of $T = 0$ K and $T = 1000$ K have been considered. Contributions to the DW term from up to third-nearest neighbors are included. There is no clear general pattern for the renormalization among the valence bands or among the conduction bands. However, in silicon the highest valence band tends to shift up and the lowest conduction band tends to shift down leading to a reduced band gap. Note that abrupt color changes are a result of the visual representation of the data and are not present in the EPR. They arise from changes in the order of bands and the finite sampling of the \mathbf{k} -point path. From a comparison of Fig. 7(a) and Fig. 7(b) it becomes apparent that for silicon an increased temperature effectively scales up the EPR. For each point in the band structure the sign of the renormalization is retained; however, the magnitude increases

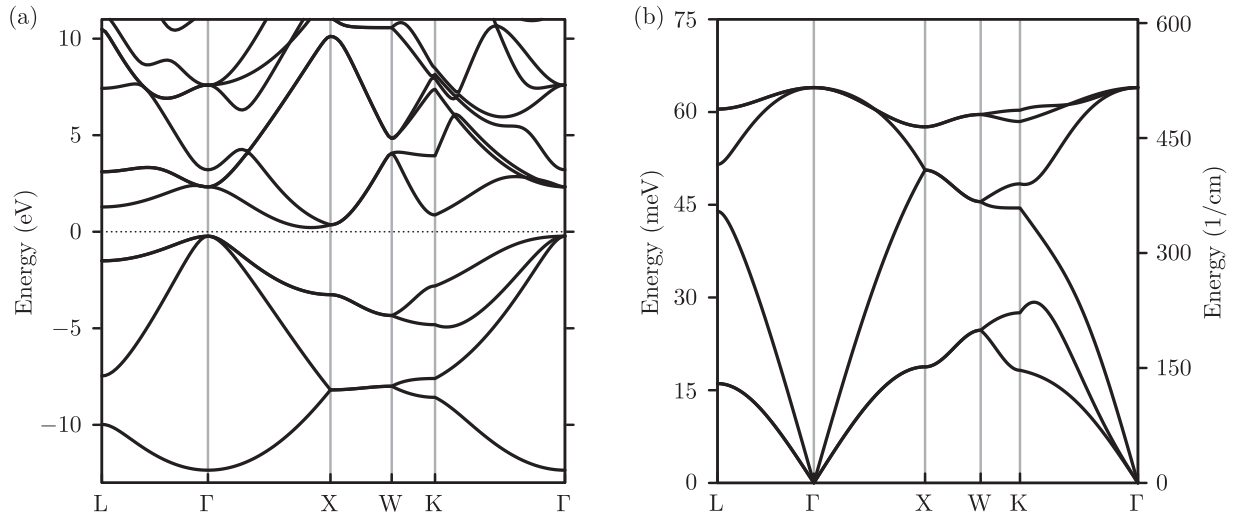


FIG. 6. (a) The band structure of bulk silicon calculated with DFT using the same basis set as the electron-phonon calculations for silicon and (b) the phonon dispersion of bulk silicon calculated with a finite-differences approach excluding $l = 3$ functions. Both results are plotted along the high-symmetry points and the zero level is set at the computed thermodynamic limit of the Fermi level.

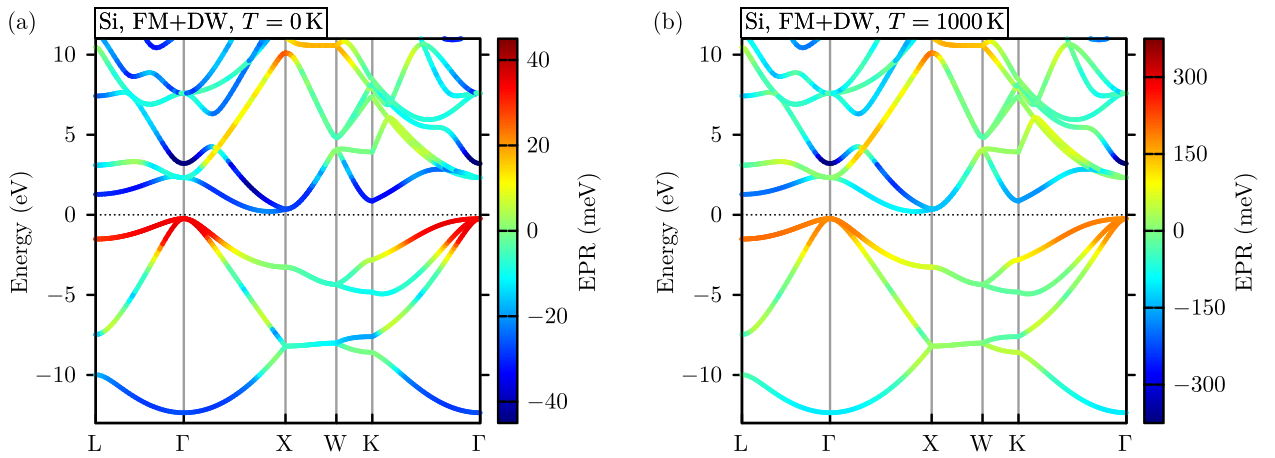


FIG. 7. The color on top of the original DFT band structure of silicon indicates the EPR of the band structure along the high-symmetry points at temperatures of (a) $T = 0$ K and (b) $T = 1000$ K including contributions to the DW component up to third-nearest neighbors.

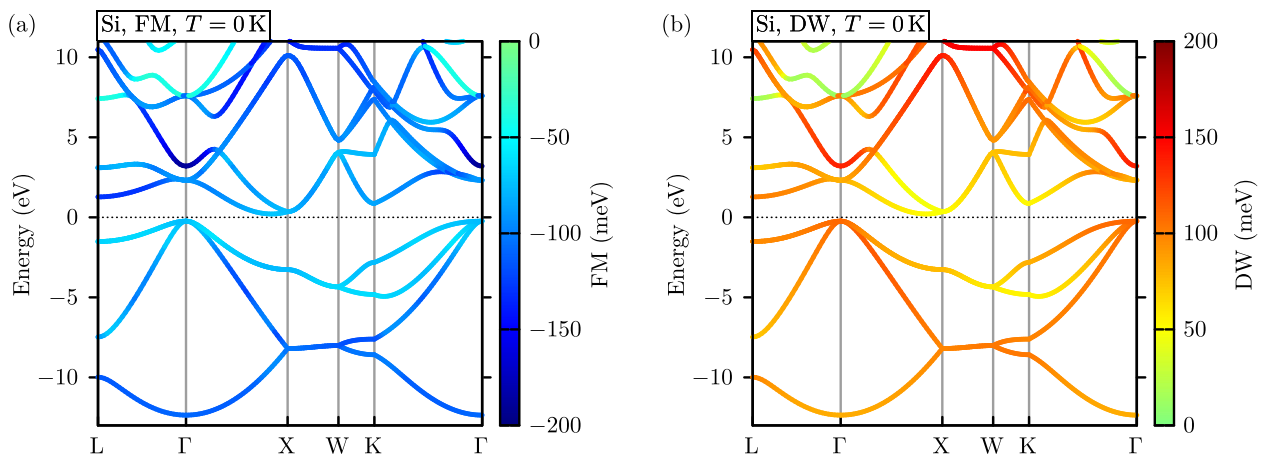


FIG. 8. The color on top of the original DFT band structure of silicon indicates the contribution of (a) the FM term [Eq. (16)] and (b) the DW term [Eq. (17)] to the EPR of the band structure along the high-symmetry points at $T = 0$ K.

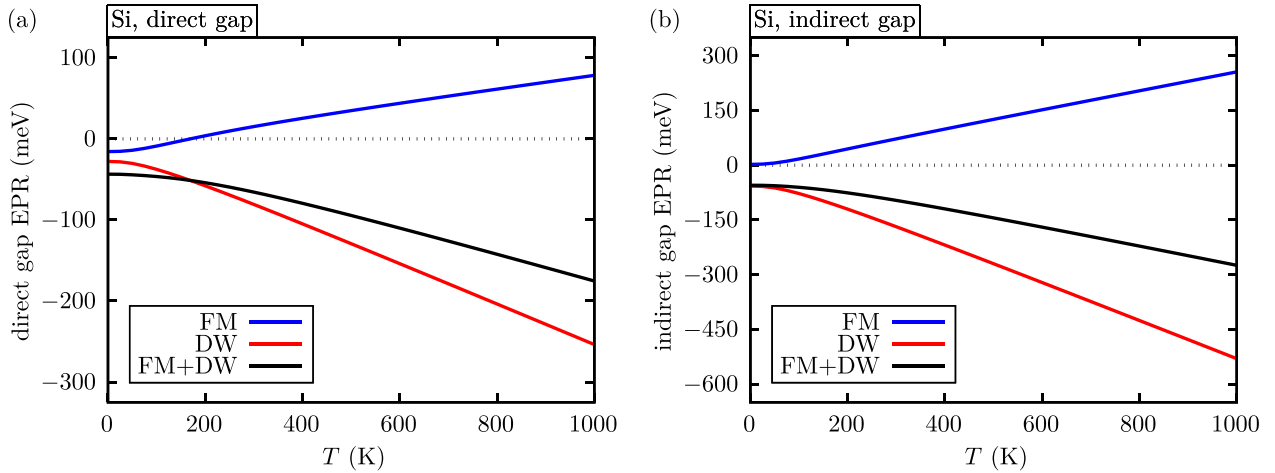


FIG. 9. The temperature dependence of the renormalization of (a) the direct band gap and (b) the indirect band gap for silicon including contributions to the DW component up to third-nearest neighbors.

as can be seen from the scaled color bar. This effective scaling factor is not uniform along the band structure and depends on the particular state and \mathbf{k} point.

The renormalization of the electronic band structure is composed of the two components $\Delta E_{nk}^{\text{FM}}$ and $\Delta E_{nk}^{\text{DW}}$ according to Eq. (18). Figure 8 shows each component separately at a temperature of 0 K. For the DW component the contributions up to third-nearest neighbors have been included. For the shown bands in the band structure of silicon, the FM component is strictly negative and the DW component is strictly positive. Since their magnitude is similar, it is important to include both components in order to obtain a physically meaningful result for the renormalization of the band structure. In this light we agree with Baumann [65] highlighting this complementary nature of both components.

The FM and DW components in silicon are not only complementary for the individual band of the electronic band structure but also for the derived band gap. In Figs. 9(a) and 9(b) the temperature-dependent EPR of the direct and the indirect band gap for silicon is displayed, respectively. Here the two components of the EPR of the band gap have an opposite dependence on the temperature. Therefore, they partly cancel each other. For silicon, the dependence of the DW component on the temperature is dominant. Thus, the band gap reduces with rising temperature.

The calculations presented above include contributions to the DW term beyond the RIA. Within the RIA, only the contributions with $(\kappa, p) = (\kappa', p')$ in the sums of Eqs. (11) and (13) are taken into account and any further contributions are neglected. The latter can be classified by the neighbor relation of the two involved atoms indicated by (κ, p) and (κ', p') . In Table I we consider the highest valence band (VB) and the lowest conduction band (CB) in silicon at the high-symmetry points to compare the different contributions to the ZPR. The contributions from different shells of nearest neighbors to the DW term decrease with an increasing number of the shell. The contributions from first-nearest neighbors are small but not necessarily negligible. They are comparable in size to the numerical uncertainties arising in the practical implementation of the underlying theory. Therefore, attempts to increase the

accuracy of electron-phonon calculations should also consider incorporating contributions from first-nearest neighbors. In the example of silicon their signs tend to be opposite to the RIA contribution such that the DW component is reduced. This reduction amounts to a noticeable fraction of the total EPR. Judging from our calculations for silicon contributions from higher shells of nearest neighbors seem to be negligible. Including contributions to the DW term beyond the RIA does not only change the EPR of the electronic band structure, but also the temperature dependence of the EPR for its band gap. In Fig. 10(a) and Fig. 10(b) the temperature dependence of the EPR for the direct and the indirect band gap is plotted, respectively. The different curves include contributions up to different shells of nearest neighbors. Including contributions up to first-nearest neighbors makes the slope of the curve for the direct band gap less steep, i.e., the direct band gap decreases more slowly when the temperature rises. Contributions from further shells of nearest neighbors have only a minor influence on the slope. For the indirect band gap

TABLE I. The ZPR in bulk silicon for the highest valence band (VB) and the lowest conduction band (CB) at the high-symmetry points broken down into its components. The DW term is further split into its RIA contribution DW_0 and further contributions DW_1 , DW_2 , and DW_3 from first-, second-, and third-nearest neighbors, respectively. All values are given in meV.

\mathbf{k}	Band	FM	DW_0	DW_1	DW_2	DW_3	Sum
L	VB	-66.79	97.73	-2.56	0.31	0.19	28.88
	CB	-128.91	100.62	-1.75	0.28	0.17	-29.59
Γ	VB	-75.10	110.69	-2.77	0.33	0.20	33.35
	CB	-90.80	81.78	-1.56	0.23	0.15	-10.20
X	VB	-76.75	78.89	-2.45	0.28	0.18	0.15
	CB	-74.78	50.02	-2.01	0.19	0.13	-26.45
W	VB	-64.27	59.57	-2.40	0.25	0.16	-6.69
	CB	-71.27	73.97	-2.25	0.22	0.15	0.82
K	VB	-75.48	82.48	-2.47	0.29	0.18	5.00
	CB	-83.68	53.77	-2.00	0.20	0.14	-31.57

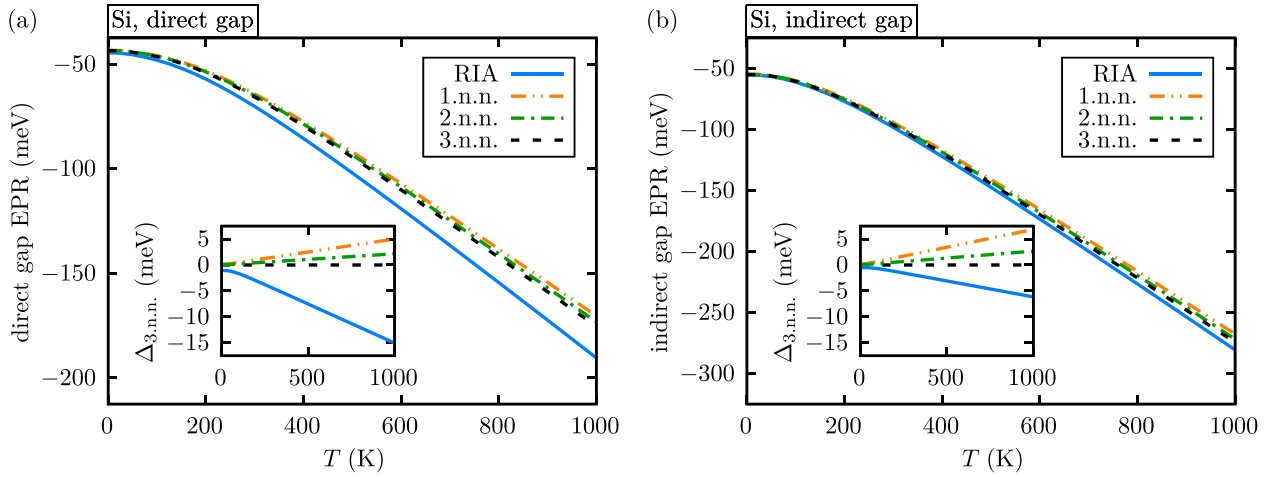


FIG. 10. The temperature dependence of the renormalization of (a) the direct band gap and (b) the indirect band gap for silicon including contributions up to different shells of nearest neighbors. The RIA curve contains only RIA contributions to the DW component, whereas 1.n.n., 2.n.n., and 3.n.n. include contributions up to first-, second-, and third-nearest neighbors, respectively. The quantity $\Delta_{3.n.n.}$ presented in the insets describes the difference of each result to the result that includes contributions up to third-nearest neighbors.

contributions from nearest neighbors have the same effect on the slope, but their influence is less significant. Poncé *et al.* [66] have previously investigated contributions beyond the RIA using a finite-differences approach. Overall, we find that the orders of magnitude are similar, even if it is difficult to directly compare these results to our calculations. Reference [66] presents contributions from specific \mathbf{q} points instead of a converged average over the Brillouin zone and uses an approach that differs from our approach. Furthermore, the use of a different pseudopotential might change the decomposition of the total electron-phonon renormalization into FM and DW contributions, even if the total renormalization agrees well [49]. In Tables II and III we list our results for the ZPR of the band gap and the asymptotic slope of its temperature dependence at high temperature including contributions up to different shells of nearest neighbors. We compare these to reference values from Ref. [7], which are based on the nonadiabatic AHC theory like our results and rely on the RIA. Therefore, these values can directly be compared to our results on the level of the RIA. For different approaches similar values can be found in the literature. A calculation based on the adiabatic AHC theory finds -47.1 and -64.3 meV for the ZPR of the direct and the indirect band gap, respectively [7]. With the frozen-phonon approach a ZPR of -60.0 meV can be found for the indirect band gap [67]. An experimen-

tal investigation yields a ZPR of -62 or -64 meV for the indirect band gap depending on the measurement technique [68]. The experimentally determined asymptotic slope of the indirect band gap is -0.32 meV/K [68]. Our results agree well with the calculations from the literature. In terms of relative deviations the asymptotic slope appears to be more sensitive to numerical variations than the ZPR. The calculated theoretical predictions underestimate the ZPR and the asymptotic slope compared to the experimental results. Including contributions from nearest neighbors changes the considered quantities only slightly and does not improve the agreement with experiments. Therefore we attribute the remaining gap between theoretical predictions and experimental findings to many-body effects [23,52] and anharmonic effects [23,30] missing from our DFT calculations.

B. Diamond

The results for diamond have been obtained using a basis set of Gaussians with three different decay constants that is similar to the basis set used for silicon. We obtain a relaxed lattice constant of 3.525 Å. This is 1.2% smaller than the experimental findings of 3.567 Å [57]. The electronic band structure of diamond can be seen in Fig. 11(a). The direct band gap has a size of 5.719 eV and the size of the indirect

TABLE II. The ZPR of the direct and indirect band gap in bulk silicon including contributions to the DW component up to different shells of nearest neighbors. The RIA result contains only RIA contributions, whereas 1.n.n., 2.n.n., and 3.n.n. include contributions up to first-, second-, and third-nearest neighbors, respectively. The results from Ref. [7] rely on the RIA and should therefore be compared with our results in the RIA. All values are given in meV.

Band gap	RIA [7]	RIA	1.n.n.	2.n.n.	3.n.n.
Direct	-42.1	-44.61	-43.40	-43.49	-43.54
Indirect	-56.2	-55.42	-54.72	-54.85	-54.91

TABLE III. The asymptotic slope of the temperature dependence of the band gap for bulk silicon at high temperatures including contributions to the DW component up to different shells of nearest neighbors. The RIA result contains only RIA contributions, whereas 1.n.n., 2.n.n., and 3.n.n. include contributions up to first-, second-, and third-nearest neighbors, respectively. The results from Ref. [7] rely on the RIA and should therefore be compared with our results in the RIA. All values are given in meV/K.

Asymp. slope	RIA [7]	RIA	1.n.n.	2.n.n.	3.n.n.
Direct	-0.147	-0.185	-0.165	-0.167	-0.170
Indirect	-0.255	-0.275	-0.262	-0.266	-0.269

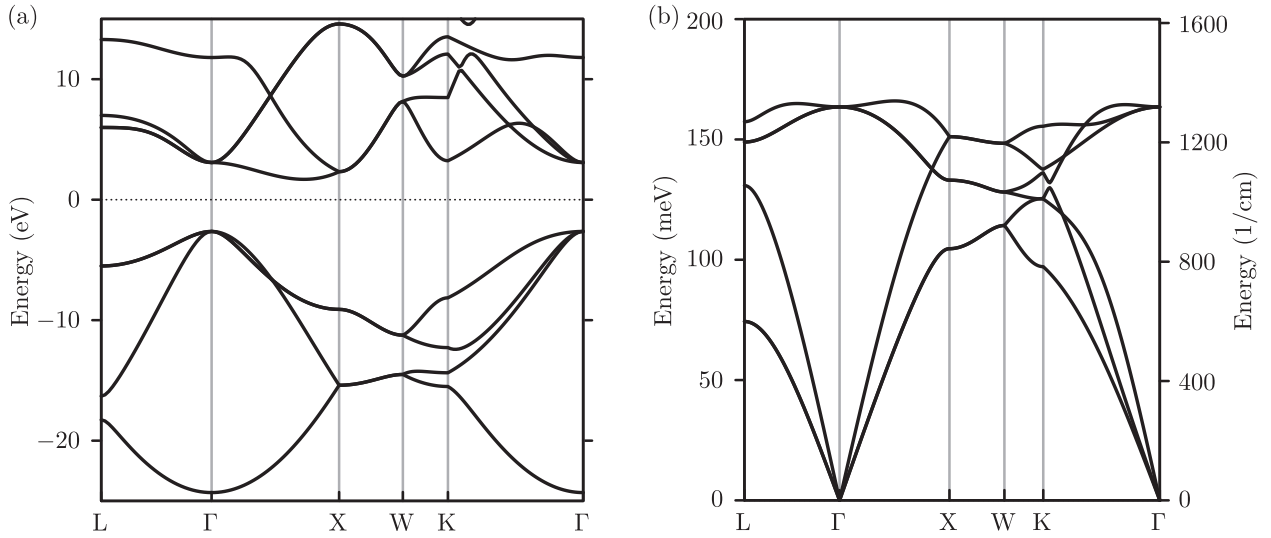


FIG. 11. (a) The band structure of diamond calculated with DFT and (b) the phonon dispersion of diamond calculated with a finite-differences approach. Similar to Fig. 6.

band gap is 4.324 eV. These results agree well with other DFT calculations [7], but like for silicon they underestimate the band gaps found in many-body calculations [58] and experiments [68], which is to be expected for a DFT calculation. The phonon dispersion of diamond is depicted in Fig. 11(b) and agrees up to about 7 meV with previous calculations [69] and measurements [62,70,71]. Thus, we can turn our attention to the EPI.

The colors on top of the original DFT band structure of diamond in Fig. 12 indicate the sign and the size of the EPR calculated using Eq. (18) for the temperatures $T = 0$ K and $T = 1000$ K. The DW term includes contributions from up to third-nearest neighbors. Again, there is no clear pattern for the renormalization among the valence bands or among the conduction bands, but the band gap is reduced by an upper valence band that tends to shift up and a lower conduction band tends to shift down. Similarly to the case of silicon, the EPR is scaled up when the temperature rises. For each point in the band structure the sign of the renormalization remains;

however, the magnitude increases. This effective scaling factor is not uniform along the band structure and depends on the particular point in the band structure. The two components ΔE_{nk}^{FM} and ΔE_{nk}^{DW} in Eq. (18) are complementary and have a similar magnitude like in the case for silicon. Table IV shows an analysis of the contributions to the ZPR in diamond broken down into the FM component and the contributions to the DW component using the example of the highest VB and the lowest CB at the high-symmetry points. For silicon and diamond we find that the contributions beyond the RIA are roughly of the same size. Again, they are small, especially compared to the size of the DW component in the RIA, which is larger in diamond than in silicon. Therefore, one might suspect that these contributions are most important in materials where the EPR is small. However, as the FM component and the DW component are complementary and largely cancel each other on the level of the RIA, contributions from first-nearest neighbors can still make up a noticeable fraction of the total EPR. For diamond the signs of these contributions are negative and

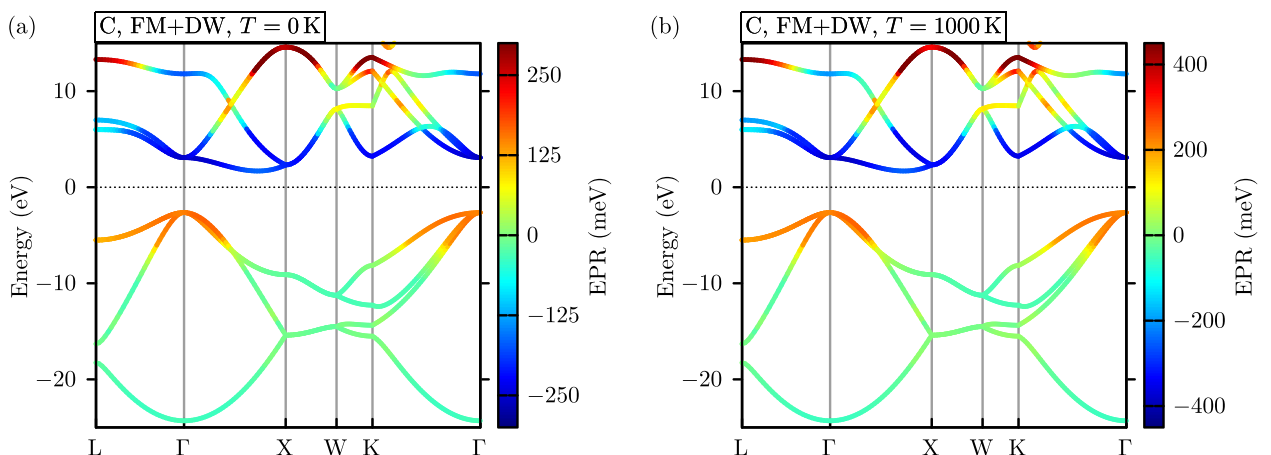


FIG. 12. The color on top of the original DFT band structure of diamond indicates the EPR of the band structure along the high-symmetry points at temperatures of (a) $T = 0$ K and (b) $T = 1000$ K including contributions to the DW component up to third-nearest neighbors.

TABLE IV. The ZPR in diamond for the highest valence band (VB) and the lowest conduction band (CB) at the high-symmetry points broken down into its components. The DW term is further split into its RIA contribution DW_0 and further contributions DW_1 , DW_2 , and DW_3 from first-, second-, and third-nearest neighbors, respectively. All values are given in meV.

k	Band	FM	DW_0	DW_1	DW_2	DW_3	Sum
L	VB	-1369.61	1494.65	-3.29	-0.37	-0.21	121.17
	CB	-1508.61	1430.19	-2.05	-0.30	-0.18	-80.95
Γ	VB	-1522.41	1674.68	-3.46	-0.42	-0.22	148.17
	CB	-1775.44	1520.43	-1.43	-0.43	-0.17	-257.04
X	VB	-1240.47	1225.63	-3.10	-0.30	-0.19	-18.43
	CB	-450.27	251.58	-2.26	-0.14	-0.16	-201.25
W	VB	-980.50	952.72	-2.85	-0.23	-0.18	-31.04
	CB	-1161.18	1231.94	-2.15	-0.23	-0.17	68.21
K	VB	-1278.08	1282.38	-3.14	-0.32	-0.19	0.65
	CB	-632.33	405.13	-2.19	-0.15	-0.16	-229.70

therefore they reduce the effect obtained within the RIA like in silicon. Contributions from further shells of nearest neighbors seem to be negligible.

Next, the effect of the contributions to the DW term beyond the RIA on the temperature dependence of the band gap is discussed. In Figs. 13(a) and 13(b) the EPR for the direct and the indirect band gap is plotted, respectively, in dependence of the temperature. The different curves in each figure include contributions up to different shells of nearest neighbors. Again, contributions beyond the RIA modify the slope of the EPR. Like for silicon, including contributions up to first-nearest neighbors makes the slope of the curve for the EPR of each band gap less steep, i.e., the band gaps decrease more slowly when the temperature rises. Contributions from further shells of nearest neighbors have less influence on the slope. The size of the corrections from first-nearest neighbors in diamond is similar to their size in silicon. Due to the significantly larger size of the band gap EPR in dia-

TABLE V. The ZPR of the direct and indirect band gap in diamond including contributions to the DW component up to different shells of nearest neighbors. The RIA result contains only RIA contributions, whereas 1.n.n., 2.n.n., and 3.n.n. include contributions up to first-, second-, and third-nearest neighbors, respectively. The results from Ref. [7] rely on the RIA and should therefore be compared with our results in the RIA. All values are given in meV.

Band gap	RIA [7]	RIA	1.n.n.	2.n.n.	3.n.n.
Direct	-415.8	-407.30	-405.28	-405.28	-405.24
Indirect	-329.79	-315.05	-313.94	-313.69	-313.65

mond their relative size is smaller and therefore they can be considered as less significant. In Tables V and VI we list our results for the ZPR of the band gap and the asymptotic slope of its temperature dependence at high temperature including contributions up to different shells of nearest neighbors. The given reference values from Ref. [7] were calculated based on the nonadiabatic AHC theory like our results and rely on the RIA. Therefore, these values can directly be compared to our results on the level of the RIA. For different approaches similar values can be found in the literature. Calculations based on the adiabatic AHC theory find -438.6 meV [7] or -409 meV [49] for the direct band gap and -379.3 meV [7] for the indirect band gap. With the frozen-phonon method a ZPR of -334 meV can be found for the indirect band gap [67]. Experimental studies yield a ZPR of -364 meV [68], -370 meV [68], or -410 meV [72] for the indirect band gap. Note that the experimental results depend heavily on the extrapolation scheme. The same experimental data can result in a ZPR of -290 meV or even -510 meV for the indirect band gap of diamond [72]. The experimentally determined asymptotic slope of the indirect band gap is -0.54 meV/K [68]. Again, our results agree well with other calculations in the literature. The deviations for the ZPR and the slope for diamond are larger than for silicon. However, the size of the effects in diamond are also significantly larger in size than the

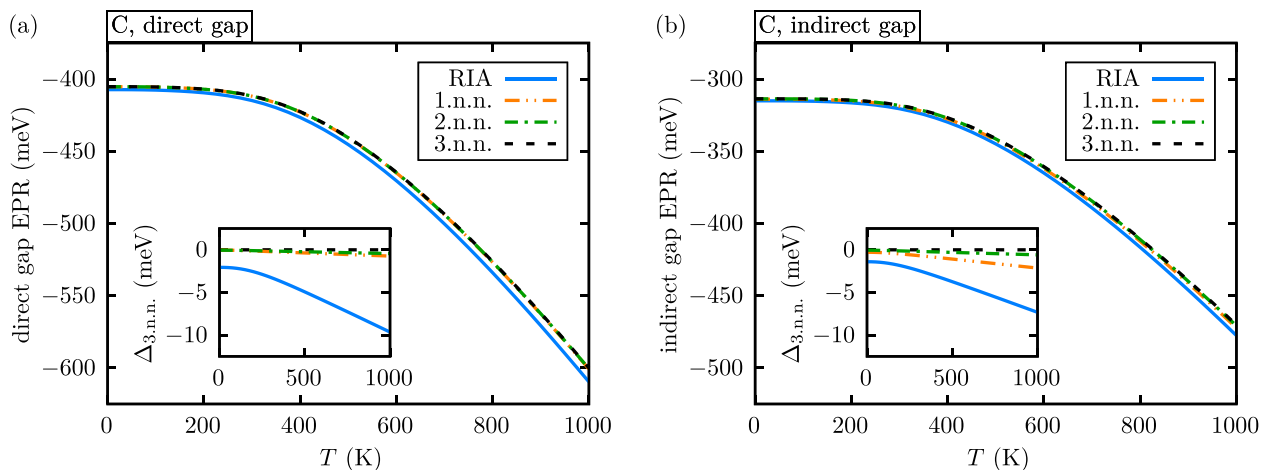


FIG. 13. The temperature dependence of the renormalization of (a) the direct band gap and (b) the indirect band gap for diamond including contributions up to different shells of nearest neighbors. The RIA curve contains only RIA contributions to the DW component, whereas 1.n.n., 2.n.n., and 3.n.n. include contributions up to first-, second-, and third-nearest neighbors, respectively. The quantity $\Delta_{3.n.n.}$ presented in the insets describes the difference of each result to the result that includes contributions up to third-nearest neighbors.

TABLE VI. The asymptotic slope of the temperature dependence of the band gap for diamond at high temperatures including contributions to the DW component up to different shells of nearest neighbors. The RIA result contains only RIA contributions, whereas 1.n.n., 2.n.n., and 3.n.n. include contributions up to first-, second-, and third-nearest neighbors, respectively. The results from Ref. [7] rely on the RIA and should therefore be compared with our results in the RIA. All values are given in meV/K.

Asymp. slope	RIA [7]	RIA	1.n.n.	2.n.n.	3.n.n.
Direct	-0.504	-0.471	-0.462	-0.462	-0.461
Indirect	-0.435	-0.381	-0.376	-0.374	-0.374

effects in silicon. The relative deviations are still comparable. Also in diamond the asymptotic slope appears to be more sensitive to numerical variations than the ZPR. Compared to the experimental reference value of -410 meV [72] for the indirect band gap our calculated theoretical predictions again underestimate the ZPR. The same holds for the asymptotic slope. Corrections due to contributions from nearest neighbors change the calculated values for the considered quantities only slightly and do not improve the agreement with experiments. Even though the experimental findings seem to be subject to noticeable uncertainties, we suspect that many-body effects [23,52] and anharmonic effects [23,30] that have been neglected in our DFT calculations play a noticeable role in the electron-phonon interaction in diamond that might explain the deviation between theory and experiment.

VII. SUMMARY

In this work we presented the calculated renormalization of the electronic band structures and band gaps of silicon and diamond due to electron-phonon interaction at different temperatures. To this end, we employed the nonadiabatic AHC theory. Our *ab initio* implementation is based on finite-differences calculations in supercells and makes use of a basis set of localized Gaussian orbitals. We report good

agreement with other implementations from the literature. We can calculate contributions to the DW component beyond the RIA, which are usually neglected in perturbative approaches in the literature. We carried out calculations considering contributions from up to third-nearest neighbors, which indicate that contributions from first-nearest neighbors are not generally negligible. The contributions tend to decrease in magnitude with increasing shells of nearest neighbors. For silicon the calculated zero-point renormalization of the direct band gap is -43.54 meV and for the indirect band gap we have -54.91 meV. At high temperature, the band gaps decrease at a rate of -0.170 and -0.269 meV/K, respectively. For diamond the calculated zero-point renormalizations are -405.24 meV for the direct band gap and -313.65 meV for the indirect band gap. At high temperature, the band gaps decrease by -0.461 and -0.374 meV/K, respectively. These results underestimate the EPR compared to experimental findings. We attribute the remaining deviations after going beyond the RIA to many-body effects and anharmonic effects. The computational effort of our implementation is moderate as it circumvents the typical computational bottlenecks discussed in the literature. Thus, it might be suitable for performing electron-phonon calculations in large and complicated systems.

ACKNOWLEDGMENTS

T.D. acknowledges financial support from the Deutsche Forschungsgemeinschaft (DFG, German Research Foundation) through Project No. 426726249 (DE 2749/2-1 and DE 2749/2-2). M.R. acknowledges financial support from the Deutsche Forschungsgemeinschaft (DFG, German Research Foundation) through Project A13 of SFB 1083. The authors gratefully acknowledge the Gauss Centre for Supercomputing e.V. (www.gauss-centre.eu) for funding this project by providing computing time through the John von Neumann Institute for Computing (NIC) on the GCS Supercomputer JUWELS [73] at Jülich Supercomputing Centre (JSC).

-
- [1] F. Giustino, Electron-phonon interactions from first principles, *Rev. Mod. Phys.* **89**, 015003 (2017).
 - [2] P. Hohenberg and W. Kohn, Inhomogeneous electron gas, *Phys. Rev.* **136**, B864 (1964).
 - [3] W. Kohn and L. J. Sham, Self-consistent equations including exchange and correlation effects, *Phys. Rev.* **140**, A1133 (1965).
 - [4] L. Hedin, New method for calculating the one-particle Green's function with application to the electron-gas problem, *Phys. Rev.* **139**, A796 (1965).
 - [5] M. Rohlfing and S. G. Louie, Electron-hole excitations and optical spectra from first principles, *Phys. Rev. B* **62**, 4927 (2000).
 - [6] M. Shishkin, M. Marsman, and G. Kresse, Accurate quasiparticle spectra from self-consistent *GW* calculations with vertex corrections, *Phys. Rev. Lett.* **99**, 246403 (2007).
 - [7] S. Poncé, Y. Gillet, J. Laflamme Janssen, A. Marini, M. Verstraete, and X. Gonze, Temperature dependence of the electronic structure of semiconductors and insulators, *J. Chem. Phys.* **143**, 102813 (2015).
 - [8] F. Karsai, M. Engel, E. Flage-Larsen, and G. Kresse, Electron-phonon coupling in semiconductors within the *GW* approximation, *New J. Phys.* **20**, 123008 (2018).
 - [9] A. Miglio, V. Brousseau-Couture, E. Godbout, G. Antonius, Y.-H. Chan, S. G. Louie, M. Côté, M. Giantomassi, and X. Gonze, Predominance of non-adiabatic effects in zero-point renormalization of the electronic band gap, *npj Comput. Mater.* **6**, 167 (2020).
 - [10] K. Kunc and R. M. Martin, *Ab initio* force constants of GaAs: A new approach to calculation of phonons and dielectric properties, *Phys. Rev. Lett.* **48**, 406 (1982).
 - [11] P. K. Lam, M. M. Dacorogna, and M. L. Cohen, Self-consistent calculation of electron-phonon couplings, *Phys. Rev. B* **34**, 5065 (1986).
 - [12] B. Monserrat, Electron-phonon coupling from finite differences, *J. Phys.: Condens. Matter* **30**, 083001 (2018).

- [13] M. Zacharias and F. Giustino, Theory of the special displacement method for electronic structure calculations at finite temperature, *Phys. Rev. Res.* **2**, 013357 (2020).
- [14] P. B. Allen and V. Heine, Theory of the temperature dependence of electronic band structures, *J. Phys. C* **9**, 2305 (1976).
- [15] P. B. Allen and M. Cardona, Theory of the temperature dependence of the direct gap of germanium, *Phys. Rev. B* **23**, 1495 (1981).
- [16] P. B. Allen and M. Cardona, Temperature dependence of the direct gap of Si and Ge, *Phys. Rev. B* **27**, 4760 (1983).
- [17] S. Baroni, P. Giannozzi, and A. Testa, Green's-function approach to linear response in solids, *Phys. Rev. Lett.* **58**, 1861 (1987).
- [18] X. Gonze, D. C. Allan, and M. P. Teter, Dielectric tensor, effective charges, and phonons in α -quartz by variational density-functional perturbation theory, *Phys. Rev. Lett.* **68**, 3603 (1992).
- [19] S. Yu. Savrasov, Linear response calculations of lattice dynamics using muffin-tin basis sets, *Phys. Rev. Lett.* **69**, 2819 (1992).
- [20] F. Giustino, M. L. Cohen, and S. G. Louie, Electron-phonon interaction using Wannier functions, *Phys. Rev. B* **76**, 165108 (2007).
- [21] X. Gonze, P. Boulanger, and M. Côté, Theoretical approaches to the temperature and zero-point motion effects on the electronic band structure, *Ann. Phys.* **523**, 168 (2011).
- [22] N. Marzari, A. A. Mostofi, J. R. Yates, I. Souza, and D. Vanderbilt, Maximally localized wannier functions: Theory and applications, *Rev. Mod. Phys.* **84**, 1419 (2012).
- [23] G. Antonius, S. Poncé, E. Lantagne-Hurtubise, G. Auclair, X. Gonze, and M. Côté, Dynamical and anharmonic effects on the electron-phonon coupling and the zero-point renormalization of the electronic structure, *Phys. Rev. B* **92**, 085137 (2015).
- [24] L. A. Agapito and M. Bernardi, *Ab initio* electron-phonon interactions using atomic orbital wave functions, *Phys. Rev. B* **97**, 235146 (2018).
- [25] J.-M. Lihm and C.-H. Park, Phonon-induced renormalization of electron wave functions, *Phys. Rev. B* **101**, 121102 (2020).
- [26] J.-M. Lihm and C.-H. Park, Wannier function perturbation theory: Localized representation and interpolation of wave function perturbation, *Phys. Rev. X* **11**, 041053 (2021).
- [27] M. Zacharias, C. E. Patrick, and F. Giustino, Stochastic approach to phonon-assisted optical absorption, *Phys. Rev. Lett.* **115**, 177401 (2015).
- [28] M. Zacharias and F. Giustino, One-shot calculation of temperature-dependent optical spectra and phonon-induced band-gap renormalization, *Phys. Rev. B* **94**, 075125 (2016).
- [29] M. Zacharias, M. Scheffler, and C. Carbogno, Fully anharmonic nonperturbative theory of vibronically renormalized electronic band structures, *Phys. Rev. B* **102**, 045126 (2020).
- [30] M. Zacharias, G. Volonakis, F. Giustino, and J. Even, Anharmonic lattice dynamics via the special displacement method, *Phys. Rev. B* **108**, 035155 (2023).
- [31] T. van der Heide, B. Hourahine, B. Aradi, T. Frauenheim, and T. A. Niehaus, Phonon-induced band gap renormalization by dielectric dependent global hybrid density functional tight binding, *Phys. Rev. B* **109**, 245103 (2024).
- [32] M. Born and R. Oppenheimer, Zur Quantentheorie der Molekeln, *Ann. Phys.* **389**, 457 (1927).
- [33] A. A. Maradudin and S. H. Vosko, Symmetry properties of the normal vibrations of a crystal, *Rev. Mod. Phys.* **40**, 1 (1968).
- [34] E. Cannuccia and A. Marini, Zero point motion effect on the electronic properties of diamond, trans-polyacetylene and polyethylene, *Eur. Phys. J. B* **85**, 320 (2012).
- [35] A. Marini, S. Poncé, and X. Gonze, Many-body perturbation theory approach to the electron-phonon interaction with density-functional theory as a starting point, *Phys. Rev. B* **91**, 224310 (2015).
- [36] J. P. Perdew and A. Zunger, Self-interaction correction to density-functional approximations for many-electron systems, *Phys. Rev. B* **23**, 5048 (1981).
- [37] L. He, F. Liu, G. Hautier, M. J. T. Oliveira, M. A. L. Marques, F. D. Vila, J. J. Rehr, G.-M. Rignanese, and A. Zhou, Accuracy of generalized gradient approximation functionals for density-functional perturbation theory calculations, *Phys. Rev. B* **89**, 064305 (2014).
- [38] D. R. Hamann, M. Schlüter, and C. Chiang, Norm-conserving pseudopotentials, *Phys. Rev. Lett.* **43**, 1494 (1979).
- [39] G. P. Kerker, Non-singular atomic pseudopotentials for solid state applications, *J. Phys. C* **13**, L189 (1980).
- [40] L. Kleinman and D. M. Bylander, Efficacious form for model pseudopotentials, *Phys. Rev. Lett.* **48**, 1425 (1982).
- [41] D. Vanderbilt, Optimally smooth norm-conserving pseudopotentials, *Phys. Rev. B* **32**, 8412 (1985).
- [42] N. Troullier and J. Martins, Efficient pseudopotentials for plane-wave calculations, *Phys. Rev. B* **43**, 1993 (1991).
- [43] T. Frederiksen, M. Paulsson, M. Brandbyge, and A.-P. Jauho, Inelastic transport theory from first principles: Methodology and application to nanoscale devices, *Phys. Rev. B* **75**, 205413 (2007).
- [44] M. Engel, H. Miranda, L. Chaput, A. Togo, C. Verdi, M. Marsman, and G. Kresse, Zero-point renormalization of the band gap of semiconductors and insulators using the projector augmented wave method, *Phys. Rev. B* **106**, 094316 (2022).
- [45] T. Gunst, T. Markussen, K. Stokbro, and M. Brandbyge, First-principles method for electron-phonon coupling and electron mobility: Applications to two-dimensional materials, *Phys. Rev. B* **93**, 035414 (2016).
- [46] R. Heid and K.-P. Bohnen, Linear response in a density-functional mixed-basis approach, *Phys. Rev. B* **60**, R3709 (1999).
- [47] R. Heid, L. Pintschovius, W. Reichardt, and K.-P. Bohnen, Anomalous lattice dynamics of ruthenium, *Phys. Rev. B* **61**, 12059 (2000).
- [48] J. Wieferink, P. Krüger, and J. Pollmann, Improved hybrid algorithm with Gaussian basis sets and plane waves: First-principles calculations of ethylene adsorption on β -SiC (001)-(3x2), *Phys. Rev. B* **74**, 205311 (2006).
- [49] S. Poncé, G. Antonius, P. Boulanger, E. Cannuccia, A. Marini, M. Côté, and X. Gonze, Verification of first-principles codes: Comparison of total energies, phonon frequencies, electron-phonon coupling and zero-point motion correction to the gap between ABINIT and QE/Yambo, *Comput. Mater. Sci.* **83**, 341 (2014).
- [50] S. Zollner, M. Cardona, and S. Gopalan, Isotope and temperature shifts of direct and indirect band gaps in diamond-type semiconductors, *Phys. Rev. B* **45**, 3376 (1992).
- [51] F. Giustino, S. G. Louie, and M. L. Cohen, Electron-phonon renormalization of the direct band gap of diamond, *Phys. Rev. Lett.* **105**, 265501 (2010).

- [52] G. Antonius, S. Poncé, P. Boulanger, M. Côté, and X. Gonze, Many-body effects on the zero-point renormalization of the band structure, *Phys. Rev. Lett.* **112**, 215501 (2014).
- [53] C. Verdi and F. Giustino, Fröhlich electron-phonon vertex from first principles, *Phys. Rev. Lett.* **115**, 176401 (2015).
- [54] J. P. Nery and P. B. Allen, Influence of Fröhlich polaron coupling on renormalized electron bands in polar semiconductors: Results for zinc-blende GaN, *Phys. Rev. B* **94**, 115135 (2016).
- [55] A. Eiguren and C. Ambrosch-Draxl, Wannier interpolation scheme for phonon-induced potentials: Application to bulk MgB₂, W, and the (1 × 1) H-covered W(110) surface, *Phys. Rev. B* **78**, 045124 (2008).
- [56] X. Gonze, B. Amadon, G. Antonius, F. Arnardi, L. Baguet, J.-M. Beuken, J. Bieder, F. Bottin, J. Bouchet, E. Bousquet, N. Brouwer, F. Bruneval, G. Brunin, T. Cavignac, J.-B. Charraud, W. Chen, M. Côté, S. Cottenier, J. Denier, G. Geneste *et al.*, The abinitproject: Impact, environment and recent developments, *Comput. Phys. Commun.* **248**, 107042 (2020).
- [57] W. Parrish, Results of the IUCr precision lattice-parameter project, *Acta Crystallogr.* **13**, 838 (1960).
- [58] M. Rohlfing, P. Krüger, and J. Pollmann, Quasiparticle band-structure calculations for C, Si, Ge, GaAs, and SiC using gaussian-orbital basis sets, *Phys. Rev. B* **48**, 17791 (1993).
- [59] G. E. Jellison and F. A. Modine, Optical functions of silicon between 1.7 and 4.7 eV at elevated temperatures, *Phys. Rev. B* **27**, 7466 (1983).
- [60] P. Giannozzi, S. de Gironcoli, P. Pavone, and S. Baroni, *Ab initio* calculation of phonon dispersions in semiconductors, *Phys. Rev. B* **43**, 7231 (1991).
- [61] C.-R. Gerhorst, A. Neukirchen, D. A. Klüppelberg, G. Bihlmayer, M. Betzinger, G. Michalíček, D. Wortmann, and S. Blügel, Phonons from density-functional perturbation theory using the all-electron full-potential linearized augmented plane-wave method FLEUR, *Electron. Struct.* **6**, 017001 (2024).
- [62] G. Nilsson and G. Nelin, Study of the homology between silicon and germanium by thermal-neutron spectrometry, *Phys. Rev. B* **6**, 3777 (1972).
- [63] J. Kulda, D. Strauch, P. Pavone, and Y. Ishii, Inelastic-neutron-scattering study of phonon eigenvectors and frequencies in Si, *Phys. Rev. B* **50**, 13347 (1994).
- [64] D. Strauch, A. P. Mayer, and B. Dorner, Phonon eigenvectors in Si determined by inelastic neutron scattering, *Z. Phys. B* **78**, 405 (1990).
- [65] K. Baumann, On the temperature dependence of the band-gap in semiconductors, *Phys. Status Solidi B* **63**, K71 (1974).
- [66] S. Poncé, G. Antonius, Y. Gillet, P. Boulanger, J. Laflamme Janssen, A. Marini, M. Côté, and X. Gonze, Temperature dependence of electronic eigenenergies in the adiabatic harmonic approximation, *Phys. Rev. B* **90**, 214304 (2014).
- [67] B. Monserrat and R. J. Needs, Comparing electron-phonon coupling strength in diamond, silicon, and silicon carbide: First-principles study, *Phys. Rev. B* **89**, 214304 (2014).
- [68] M. Cardona and M. L. W. Thewalt, Isotope effects on the optical spectra of semiconductors, *Rev. Mod. Phys.* **77**, 1173 (2005).
- [69] P. Pavone, K. Karch, O. Schütt, W. Windl, D. Strauch, P. Giannozzi, and S. Baroni, *Ab initio* lattice dynamics of diamond, *Phys. Rev. B* **48**, 3156 (1993).
- [70] J. L. Warren, J. L. Yarnell, G. Dolling, and R. A. Cowley, Lattice dynamics of diamond, *Phys. Rev.* **158**, 805 (1967).
- [71] S. A. Solin and A. K. Ramdas, Raman spectrum of diamond, *Phys. Rev. B* **1**, 1687 (1970).
- [72] B. Monserrat, G. J. Conduit, and R. J. Needs, Extracting semiconductor band gap zero-point corrections from experimental data, *Phys. Rev. B* **90**, 184302 (2014).
- [73] D. Alvarez (Juelich Supercomputing Centre), JUWELS Cluster and Booster: Exascale Pathfinder with Modular Supercomputing Architecture at Juelich Supercomputing Centre, *J. Large-Scale Res. Facilities* **7**, A183 (2021).